Mechanical behaviours of concrete segmented tunnel considering the effects of grouting voids

A 3D numerical simulation

Bao, Xiaohua; Wu, Xianlong; Zhang, Xuehui; Shen, Jun; Chen, Xiangsheng; Dang, Pengliang; Cui, Hongzhi

DOI
10.1016/j.cscm.2025.e04370

Publication date
2025

Document Version
Final published version

Published in
Case Studies in Construction Materials

Citation (APA)
Bao, X., Wu, X., Zhang, X., Shen, J., Chen, X., Dang, P., & Cui, H. (2025). Mechanical behaviours of concrete segmented tunnel considering the effects of grouting voids: A 3D numerical simulation. *Case Studies in Construction Materials*, *22*, Article e04370. https://doi.org/10.1016/j.cscm.2025.e04370

Case Studies in Construction Materials 22 (2025) e04370

Contents lists available at ScienceDirect

Case Studies in Construction Materials

journal homepage: www.elsevier.com/locate/cscm

Mechanical behaviours of concrete segmented tunnel considering the effects of grouting voids — A 3D numerical simulation

Xiaohua Bao [a,b], Xianlong Wu [a,b], Xuehui Zhang [c,d,*], Jun Shen [a,b], Xiangsheng Chen [a], Pengliang Dang [e], Hongzhi Cui [a,b]

[a] State Key Laboratory of Intelligent Geotechnics and Tunnelling, College of Civil and Transportation Engineering, Shenzhen University, Shenzhen, Guangdong 518060, China
[b] Key Laboratory of Coastal Urban Resilient Infrastructures (Shenzhen University), Ministry of Education, Shenzhen 518060, China
[c] Geo-Engineering Section, Department of Geo-science and Engineering, Delft University of Technology, Delft, the Netherlands
[d] Department of Civil and Environmental Engineering, The Hong Kong Polytechnic University, Hung Hom, Kowloon, Hong Kong SAR
[e] Sinohydro Bureau 14 Co. LTD., Dali, Yunnan 671000, China

ARTICLE INFO

Keywords:
Shield tunnel
Concrete segments
Grouting voids
Mechanical performance
Stress concentration

ABSTRACT

Concrete segments are commonly utilized as linings in shield tunnels to support the load from the surrounding ground, with their mechanical performance playing a crucial role in ensuring tunnel safety. During the construction of shield tunnels, these segments are assembled on-site, and grouting is performed concurrently to promptly fill the gap between the segment and the surrounding ground. However, inadequate grouting can lead to the formation of voids, which are hidden construction defects that compromise the mechanical stability of the tunnel segments. This study explores the impact of grouting voids on the mechanical performance of concrete segmental tunnels during construction using a 3D numerical simulation. A 3D finite-element model of a segmented shield tunnel with grouting voids was developed based on the load-structure method. The analysis focused on the effects of void characteristics, such as their angle, position, and length, on the tunnel's mechanical behavior. The results indicate that voids located at the tunnel crown reduce the vertical convergence of the tunnel cross-section, while voids at the waist exacerbate its horizontal convergence. Additionally, the presence of voids alters the bending moment distribution in the segments. Compared to the case without a void, there is a reversal of the bending moment when the void is located at the crown, and the bending moment increases from −13 kN·m to 24 kN·m, potentially causing tensile damage. Furthermore, voids also induce stress concentration within the segments, and the maximum stress concentration factor (SCF) occurs at the center of the voids as 2.44. However, when a circumferential joint intersects the void, joint opening causes stress redistribution, with the most significant stress concentration appearing at 45° on both sides of the void. These findings contribute to better damage recognition and enhance the safety assurance of concrete shield tunnels.

* Corresponding author at: Geo-Engineering Section, Department of Geo-science and Engineering, Delft University of Technology, Delft, the Netherlands.
E-mail address: X.Zhang-10@tudelft.nl (X. Zhang).

https://doi.org/10.1016/j.cscm.2025.e04370
Received 17 September 2024; Received in revised form 25 December 2024; Accepted 6 February 2025
Available online 8 February 2025

1. Introduction

1.1. Shield tunnel

Building tunnels is an important way to expand usable space underground in densely populated cities, which can mitigate ground congestion issues. Among various tunnel construction methods, the shield (or boring) method has been widely used in urban tunnel construction owing to its ease of controlling ground disturbance, high adaptability to various ground types, and long-distance tunnelling capacity [1,2], which makes it well-suited especially in urban tunnelling projects [3,4].

Shield tunnel linings are typically composed of precast segments, primarily made of reinforced concrete, which are assembled and connected with steel bolts in both circumferential and radial directions [5–8]. A simplified illustration of shield tunnel construction is provided in Fig. 1(a). In general, a specialized shield machine is used for soil excavation and removal, providing temporary support through its external shell in the tunnelling section to counter the soil and water pressure from the surrounding strata, while also ensuring a safe working environment inside the machine [9–11]. Once an excavation step is completed by the shield cutterhead, concrete segments are assembled piece by piece to form the full tunnel lining. Because of the thickness of the shield shell, a gap is formed between the segment and the stratum during the shield advancement process [12]. To ensure good contact between the segment and the stratum, while also preventing excessive ground, the grout mixture, mainly consisting of cement, fly ash, etc., is synchronously injected into the gap [13,14], and this creates a grouting layer around the shield tunnel [15,16] as indicated in Fig. 1. Additionally, the fluid grout fills the pores or cracks in the surrounding stratum, thus sealing the groundwater flow channels [17,18].

1.2. Effects of grouting voids on concrete tunnel safety

As the tunnel lining is embedded into the circumferential grouting layer, the quality of the grouting layer, such as its compactness and stiffness, directly affects the shield tunnel structure behaviours and long-term safety. Therefore, assuring qualified grouting work has always been a critical part of the work of tunnel engineers. Generally, in shield tunnelling, grouting quality is ensured by properly controlling the grouting volume and pressure [19], and non-destructive testing methods are also used to check the uniformness of the grouting layer, such as ground-penetrating radar and frequency monitoring [20,21]. However, none of these methods can guarantee that the grouting layer is dense and meets the design requirements, and voids may still appear in the grouting layer. The reasons may be as follows: (a) grout flows towards the bottom of the tunnel under gravity, which causes the crown area to be vulnerable to soil loosening [22]; (b) during synchronous grouting, the groundwater can enter the grouting layer and form blisters, and voids are formed with the evaporation of water [23], and (c) an unreasonable grout ratio causes the slurry to shrink significantly during solidification [24].

Voids within the grouting layer, known as grouting voids, can create pathways for groundwater flow, thereby compromising the waterproofing effectiveness of shield tunnels, particularly in offshore or undersea tunnel projects [25,26]. In addition, these voids significantly impact the mechanical behavior of the shield tunnel by disrupting the continuous contact between the concrete segments and the surrounding ground, leading to stress concentrations [27,28]. Over time, this can accelerate the aging of the segments under sustained loads and decrease their overall durability [20,29]. The presence of a grouting void alters the transfer mode of loads between the segments and strata. Field investigations have established a clear correlation between grouting voids and segment damage. Yasuda et al. [30,31] derived an elastic solution to describe the deformation of circular tunnels influenced by grouting voids. Qin et al. [32] examined the impact of grouting void location on the performance and safety of segment joints, revealing that voids at the tunnel shoulder and springline increase the likelihood of the tunnel adopting an elliptical shape. Min et al. [33] investigated the effect of grouting voids on tunnel cracking, finding that the spatial distribution of longitudinal cracks is closely linked to the size of the voids. Zhang et al. [34] explored the impact of grouting void-induced cracks and concluded that these cracks can lead to brittle damage, which significantly reduces the bearing capacity of the tunnel structure. Leung et al. [35] studied the influence of grouting voids on axial forces and bending moments in circular tunnels, discovering that voids can reverse bending moments when the loosened area exceeds 10 % of the tunnel's circumference.

Previous studies have primarily focused on the effects of voids during the operational phase of shield tunnels, aiming to offer insights for repairing tunnel defects and extending their service life [30–35]. However, many voids are formed during the synchronous

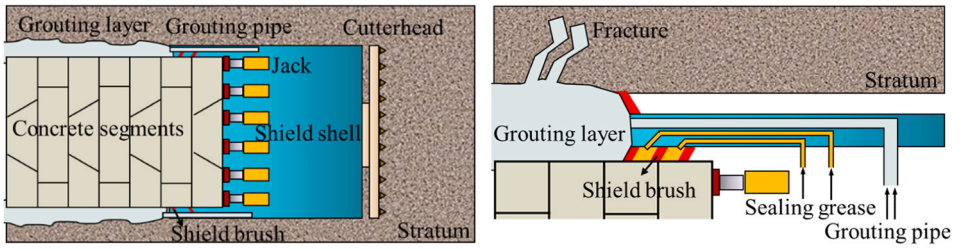

Fig. 1. Typical shield tunnel construction schematic.

grouting phase, and their impact on the tunnel structure begins in the construction stage. This differs from the plane-strain conditions typically observed in the operational phase. During construction, shield tunnels are subjected to various forces, including jack thrust, wire brush pressure, and grouting pressure, leading to a more complex, three-dimensional stress state in the tunnel segments. The stress state and concentration within the tunnel segments also undergo significant changes. When the stress alterations caused by grouting voids are combined with the complex load conditions present during construction, unexpected damage to the segments can occur. Furthermore, many previous studies have relied on two-dimensional numerical models, which are unable to fully account for the three-dimensional spatial effects of grouting voids, including both circumferential and longitudinal distributions. To address this limitation, this study developed a three-dimensional numerical simulation model to investigate the impact of grouting voids on the mechanical behavior of segments during the construction phase of shield tunnels.

1.3. Contributions and innovations

Given the limitations of the above-mentioned studies, this study conducts an in-depth analysis of the effects of grouting voids on tunnel structure. The key innovations of this study are: (1) the use of a 3D numerical model, which offers more accurate structural simulation compared to earlier studies; (2) the simultaneous consideration of multiple construction loads, including jack thrust, shield brush pressure, grouting pressure, and stratum load, an improvement over previous approaches; and (3) the incorporation of various void characteristics in the simulation, such as the positions, lengths, and angles of the voids. This study offers valuable insights into the structural deformation behavior of shield tunnels affected by grouting void defects and contributes to enhancing the safety design of these structures.

The remainder of this study is organized as follows: Section 2 introduces the engineering background on which the research is based. In Section 3, a three-dimensional (3D) numerical simulation model of the concrete shield tunnel is developed, utilizing the load-structure method to simulate the mechanical behavior of the tunnel during the construction phase, while a ground spring model is employed to represent the interaction between the stratum and the concrete segments. Section 4 presents a detailed analysis and discussion of the effects of grouting voids during construction. Finally, Section 5 provides a summary of the study's conclusions.

2. Engineering background

2.1. Engineering background information

The Shenzhen Metro Line 11, located in Shenzhen, China, serves as a vital urban subway line, spanning approximately 53.11 km. This line traverses highly populated urban regions, with its tunnel primarily constructed using the shield tunneling method. As shown in Fig. 2(a), is composed of six concrete segments: one key segment (S1), two adjacent segments (S2, S6), and three standard segments

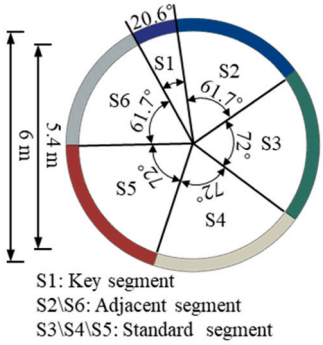

(a) Composition of shield tunnel ring

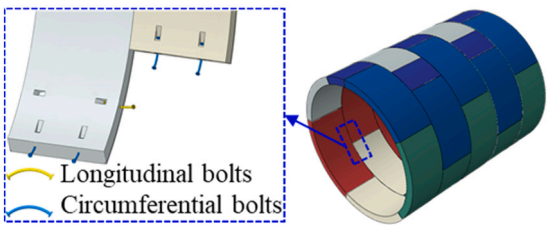

(b) Assembly method of concrete segment

Fig. 2. Concrete segments form the lining of the shield tunnel.

(S3, S4, S5). The outer diameter of the tunnel is 6 m, and the thickness of the segment is 0.3 m. The segments are assembled using high-strength bolts to finally form the shield tunnel lining, as shown in Fig. 2(b). Fig. 3 illustrates the typical construction of concrete segments. Initially, the reinforcement cage is placed into a custom steel mold (Fig. 3(a)), after which the concrete mixture is poured and cured to the designed strength in a special segment manufacturing factory (Fig. 3(b)). The manufactured concrete segments are then transported to the construction site, where they are sequentially assembled within the shield machine (Fig. 3(c)) to form finally the shield tunnel (Fig. 3(d)).

2.2. Adverse effects of grouting voids on concrete tunnel

During shield tunnel construction, the prepared grouting mixture is injected into the gap between the segment lining and the surrounding stratum to realise the transfer of strata loads to the tunnel structure. However, voids frequently form behind the lining due to the complex geological conditions and construction errors, as shown in Fig. 4. The presence of these voids, coupled with the complex construction loadings, alters the stress state of the concrete tunnel structure, leading to undesirable deformation in the lining, which may subsequently result in cracking, structural damage, and joint leakage.

3. Model establishment and calculation method

3.1. 3D Finite-element model for concrete tunnel structure

A finite-element model was established to simulate the construction process of the shield tunnel, as shown in Fig. 5. The model is longitudinally divided into 13 tunnel rings (R1 to R13), with each ring having a width of 1.5 m and a total longitudinal length of 19.5 m, as shown in Fig. 5(a). The load distribution is shown in Fig. 5(b), while the load simulating procedure for the tunnel follows the construction progress is shown in Table 1. In the initial state, only R1 to R4 are activated, with ground pressure, wire brush pressure (1.0 MPa), and jack thrust force (1.5 MPa) applied. In this study, the grouting pressure is considered to be 0.3 MPa, bases on the construction records of Metro Line 11. Considering the curing process of the grouting material, the grouting pressure decays from 0.3 MPa to 0.15 MPa and ultimately becomes equal to the ground load [36,37]. The displacement in the Z direction on the side surface of R1 was fixed to provide displacement constraints for the 3D model. As tunnel construction progresses, R5 to R13 are activated sequentially, and once R13 is activated and the jacking force is applied, the simulation of the shield tunnel construction process is completed. R6 to R8 are the primary focus of analysis in this study, as they are located at the center of the model, minimizing boundary effects.

The ground spring was used to characterise the interaction between the stratum and the concrete lining, as shown in Fig. 6. Besides, the bolts in the segment joints of the tunnel were modelled using a point-to-point bolt spring. The specific parameters for both the ground spring and bolt spring are detailed in the subsequent sections. The interaction at the interface between adjacent segments is defined as follows: (1) in the normal direction, a hard contact is applied, allowing separation after contact occurs, and (2) in the tangential direction, frictional contact is applied. Since other components at the interface, such as the concave tenon and sealing rubber, are not modeled, the friction coefficient has been appropriately increased. To balance accuracy and computational efficiency in the finite-element analysis, the friction coefficient was set to 0.5 [36,38].

3.2. Ground load simulation

The typical silty clay in the Shenzhen area was selected as the model stratigraphic condition, and its main mechanical properties are listed in Table 2.

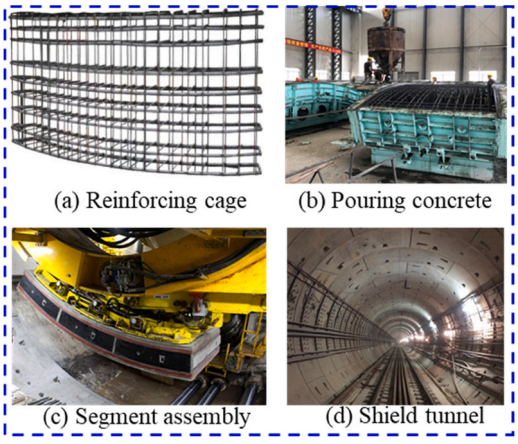

Fig. 3. Concrete segment manufacturing and field assembly for tunnel lining.

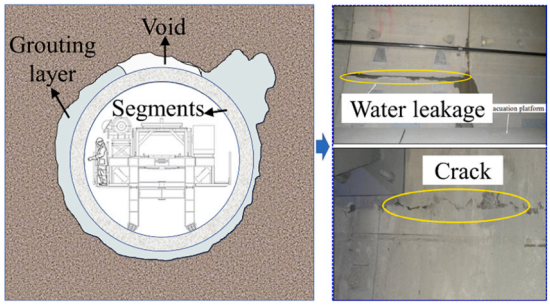

Fig. 4. Void causing damage to concrete segments (revised based on [31]).

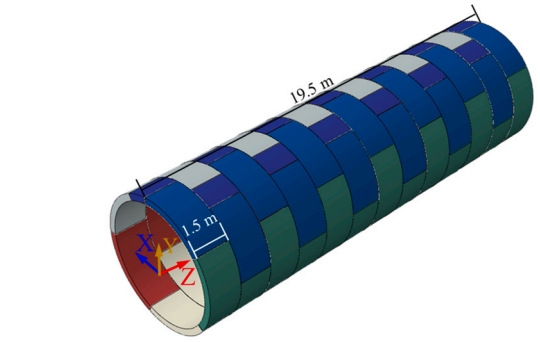

(a) Three-dimensional (3D) model of concrete shield tunnel

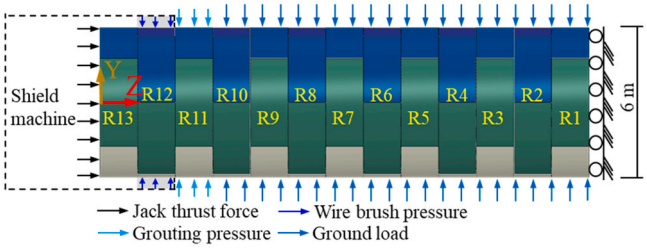

(b) Load distribution during construction

Fig. 5. Numerical simulation model for shield tunnel construction.

Table 1
Shield tunnel construction process.

Ring Step	R1	R2	R3	R4	R5	R6	R7	R8	R9	R10	R11	R12	R13
1	RA GL	RA GP	RA BP	RA JF	RD	RD	RD	RD	RD	RD	RD	RD	RD
2	RA GL	RA GL	RA GP	RA BP	RA JF	RD	RD	RD	RD	RD	RD	RD	RD
⋮	⋮												
10	RA GL	RA GL	RA GL	RA GL	RA GL	RA GL	RA GL	RA GL	RA GL	RA GL	RA GP	RA BP	RA JF

Note: RA-Ring activated; RD-Ring deactivated; GL-Ground loads; GP-Grouting pressure; BP- Brush pressure; JF-Jack (thrust) force

The tunnel was buried at a depth of 20 m, which is more than twice the outer diameter of the tunnel. In accordance with the Chinese code (GB/T 51438–2021) [39], the unloading arch effect of the soil was considered. The ground loads of each segments were calculated using Terzaghi's relaxation ground pressure theory, as shown in Fig. 7. A detailed explanation of the procedure for determining ground loads is provided in the Appendix. The ground loads are listed in Table 3.

A non-linear ground spring was used to describe the interaction between the stratum and segments. The calculation method for the

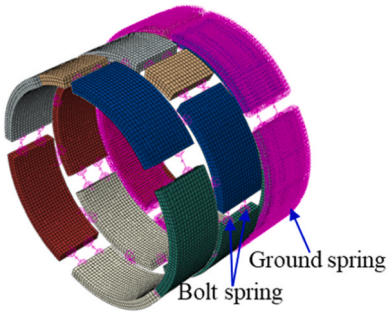

Fig. 6. Ground spring and bolt spring.

Table 2
Parameters of stratum.

Weight ($kN \cdot m^{-3}$)	Poisson's ratio	Cohesive force (kPa)	Friction angle (°)	Elastic modulus (Pa)
20.6	0.3	30	15	27×10^6

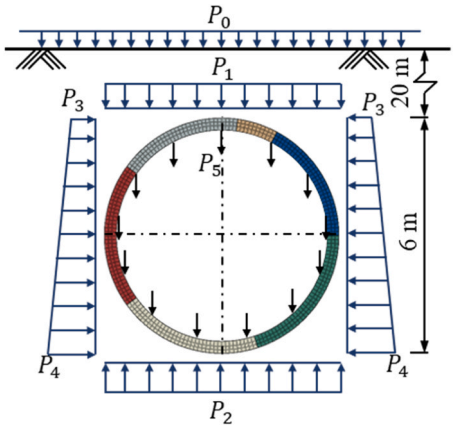

Fig. 7. Distribution of ground pressure on segments.

Table 3
Ground load specifications.

P_0/kPa	P_1/kPa	P_2/kPa	P_3/kPa	P_4/kPa
20	351.642	366	140.8	190.3

radial stiffness k_r of the ground spring is presented in Eq. (1), following the approach proposed by Wood [40], which considers the compression coefficient of the tunnel elliptical deformation. For the tangential stiffness k_s, it is assumed to be one-third of the radial stiffness, as presented in Eq. (2) [41–43].

$$k_r = \frac{3E}{R(1+\mu)(5-6\mu)} \tag{1}$$

$$k_s = \frac{1}{3}k_r \tag{2}$$

where R is the radius of the tunnel, E is the elastic modulus of the ground stratum, μ is the Poisson's ratio of the stratum.

The non-linear ground spring was applied to the element node of the mesh, with all loads applied to the segment surface in the form of pressure. Consequently, a mesh sensitivity analysis of the ground spring is required. Fig. 8 presents the radial displacement of the segment under various mesh sizes to assess this sensitivity. The radial displacement of the concrete segments decreased as the mesh

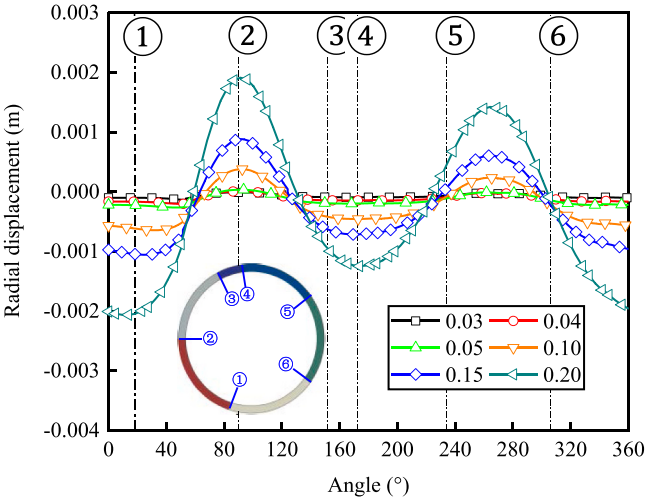

Fig. 8. Radial displacement of segments with different mesh size.

size was reduced and gradually stabilized. Considering both computational cost and the significant deformation effects observed in the shield tunnel, a mesh size of 0.20 m was selected for this study. The radial and tangential stiffness of the ground spring were 3.24×10^6 Pa/m and 1.08×10^6 Pa/m, respectively. The radial ground spring bears only compressive load and enters the plastic stage when the compression reaches 0.01 m, beyond which it cannot provide additional compression resistance. The tangential ground spring offers shear resistance in both directions and enter the plastic stage when the deformation reaches 0.003 m, as shown in Fig. 9. The plastic displacement limits of the ground spring were based on the parameters provided for soft clay layers in GB/T 50470–2017 [44].

3.3. Calculation of segment structure

3.3.1. Mechanical parameter of concrete

In this study, the strength class of concrete for the segments is C50 (concrete cubic samples with a standard compression strength of 50 MPa after 28-day curing). The concrete damage plastic (CDP) model was used to describe the mechanical properties of the concrete segment. By defining the stress-strain relationship under uniaxial tension and compression, the softening characteristics of concrete can be described [45,46], as shown in Fig. 10(a). In the CDP model, the compressive cracking and tensile cracking of concrete are represented by ε_t^{ck} and ε_t^{ck}, respectively. The compressive and tensile stress of concrete can be obtained from Eq. (3) and Eq. (4). The stiffness degradation of concrete was described using compressive damage factor d_c and the tensile damage factor d_t, and they were defined by Eq. (5) and Eq. (6).

Based on the inelastic damage relationship for concrete provided by GB50010–2010 [47] and Jin et al. [36], the mechanical parameters were determined. The specific parameters used in the finite-element analysis were listed in Table 4, and the uniaxial stress-strain relationship of C50 concrete was illustrated in Fig. 10(b). The correctness of these parameters has been validated by Liu et al. [48].

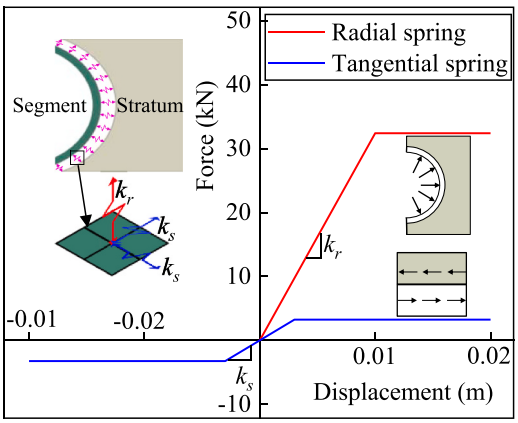

Fig. 9. Non-linear mechanical characterisation of ground spring.

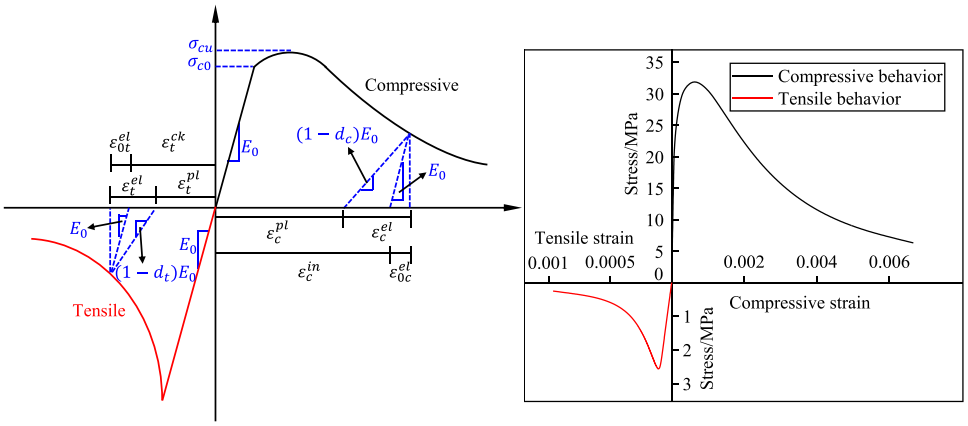

(a) Description of CDP model (b) Uniaxial stress-strain relationship of C50 concrete

Fig. 10. Constitutive relations and parameters of the CDP model.

Table 4
Concrete mechanical parameters used in the finite-element model.

Density ($kg \cdot m^{-3}$)	Elastic modulus (GPa)	Poisson ratio	Dilation angle (°)
2420	32.5	0.2	38
Eccentricity	Cohesion coefficient	f_{b0}/f_{c0}	stress ratio
0.1	0.005	1.16	0.667

$$\sigma_c = (1 - d_c)E_0(\varepsilon_c - \varepsilon_c^{pl}) \tag{3}$$

$$\sigma_t = (1 - d_t)E_0(\varepsilon_t - \varepsilon_t^{pl}) \tag{4}$$

$$d_c = 1 - \frac{\sigma_c E_0^{-1}}{\sigma_c E_0^{-1} + \varepsilon_c^{in}(1 - 1/b_c)} \tag{5}$$

$$d_t = 1 - \frac{\sigma_t E_0^{-1}}{\sigma_t E_0^{-1} + \varepsilon_t^{ck}(1 - 1/b_t)} \tag{6}$$

where σ_c, σ_t, E_0, ε_c^{pl}, ε_t^{pl} are the tensile stress, the compressive strength, the elastic modulus, the compressive equivalent plastic strain, and the tensile equivalent plastic strain.

The double-broken linear elasticity with a yield strength of 400 MPa and an ultimate strength of 500 MPa was used to describe the mechanical properties of reinforcement bars. The reinforcement bars were modeled using truss elements embedded within the concrete segments. The interaction between the concrete and reinforcement bars was modeled through a perfect bond assumption. This means that the reinforcement bars are assumed to deform together with the concrete, without slip occurring at the interface.

3.3.2. Parameter of bolt spring

In this model, type M24 bolts were used to connect adjacent segments, with a bolt inclination angle of 60°, as shown in Fig. 11. It should be noted that the hand hole and the waterproof sealing pad were not considered in the model, as their influence on shield tunnel deformation is generally considered negligible [49]. Bolt springs were used to simulate the tensile and shear behaviour of shield tunnel joints. The bolts completely bore the tensile resistance at the joint. The stiffness of the normal bolt spring k_{jn} was determined using Eq.

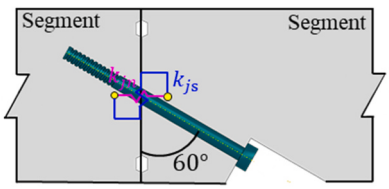

Fig. 11. Function of bolting adjacent segments.

(7) based on the method in [50], while the equivalent shear stiffness of the shear bolt spring was determined by Eq. (8).

$$k_{jn} = \frac{EA}{l}\sin\theta \tag{7}$$

where E is the elastic modulus of the bolt (640 MPa), A is the cross-sectional area of the bolt (352.5 mm^2), l is the length of the bolt (450 mm).

$$k_{js} = \frac{(kGA)_{eq}}{n}\cos\theta \tag{8}$$

where $(kGA)_{eq}$ is equivalent shear stiffness of joints, n is the number of bolts. The tensile stiffness of the bolt spring is 4.5×10^8 N/m, and the shear stiffness is 1.6×10^8 N/m.

The reliability of the 3D segment ring FEM model was validated following the full-scale load tests conducted by Lu [51]. The results of the numerical simulation were compared with the experimental data to validate the mechanical parameters and constitutive models mentioned earlier. The horizontal convergence of the haunch Δd with respect to load levels was recorded, as shown in Fig. 12. The results of the numerical simulation showed very good agreement with the full-scale test results. The error in the final horizontal convergence of haunch is only 10 mm, which is sufficiently accurate for a shield tunnel with a diameter of 6 m. Therefore, it can be concluded that the numerical simulation strategy employed in this study is reliable.

3.4. Influence parameters of grouting voids

In this study, the influence of the position, angle, and length of the void on the structural mechanical properties during the shield tunnel construction were investigated. Voids were set at the crown and waist because these two locations correspond to the points where the maximum positive and negative bending moments of the shield tunnel occur. Voids at these positions have a significant impact on the mechanical state of the shield tunnel. The circumferential extent of the voids is assumed to be symmetric along the vertical axis for crown voids and the horizontal axis for waist voids (see Fig. 13). The central angle of the arc of the circumferential void boundaries is defined as α, with the values of α are set to 18°, 36°, and 54°. The selection of void angles was based on the study by Qin et al. [28], which found that voids with different angles could alter the deformation pattern of the shield tunnel, particularly affecting the bending moment state.

Regarding the influence of the void length, l, voids with $\alpha = 36°$ were simulated at the crown and waist of R6 & R7 ($l = 3.0$ m), and R6 & R7 & R8 ($l = 4.5$ m), as shown in the Fig. 13. Voids of different lengths correspond to different health conditions of the shield tunnel [52]. In the simulation, the ground loads, grouting pressures, and ground springs within the void regions were excluded. For comparison purposes, a reference case without voids was also established, and 11 specific scenarios were designed as outlined in Table 5.

4. Results and discussion

The position, angle, and length of the void were considered when studying the displacement and mechanical characteristics of the segments during the shield tunnel construction under the negative influence of grouting voids. The simulation results are presented and discussed in subsequent sections.

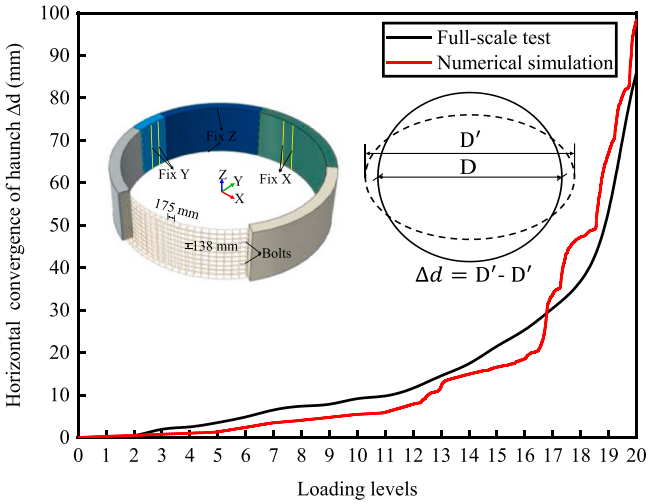

Fig. 12. Comparison of FEM and full-scale test results.

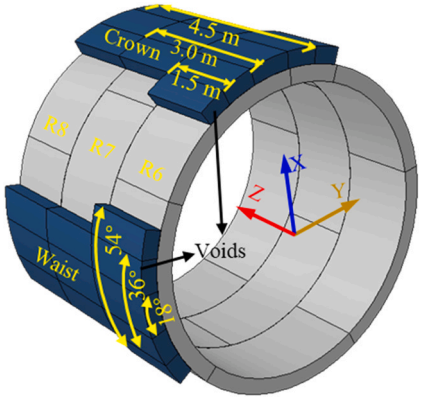

Fig. 13. Schematical illustration of void position, angle, and length.

Table 5
Analysis cases.

Case	Location	Angle, α (°)	Length, *l* (m)
Case 0	/	/	/
Case 1	Crown	18	1.5
Case 2	Crown	36	1.5
Case 3	Crown	36	3.0
Case 4	Crown	36	4.5
Case 5	Crown	54	1.5
Case 6	Waist	18	1.5
Case 7	Waist	36	1.5
Case 8	Waist	36	3.0
Case 9	Waist	36	4.5
Case 10	Waist	54	1.5

4.1. Normal case without voids

The simulation results of the segmented lining corresponding to the normal (reference) case are discussed. The vertical displacements at the crown of R1–R13 in Step 10 are shown in Fig. 14. R13–R10 are newly assembled rings and subjected to jack thrust force, wire brush pressure, grouting pressure, and ground loads, respectively. The vertical displacement slightly increased as the segment are positioned farer from the front loading end. However, it stabilizes around 1.5 mm after R9. The displacement of R6 is nearly identical to that of the adjacent segments, indicating that the deformation of R6 has stabilized. Therefore, the mechanical behavior of R6 in Step 10 was selected for detailed analysis.

The construction process of a shield tunnel without grouting void defects was simulated and labelled as Case 0. The radial

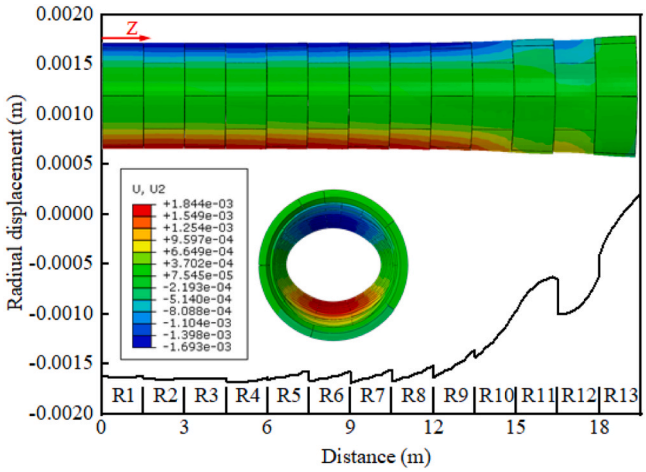

Fig. 14. Radial displacement of shield tunnel at the crown.

displacement, bending moment, and axial force of segment R6 were analyzed under various loading stages, including jack thrust force (Step 3), wire brush pressure (Step 4), grouting pressure (Step 5), ground loads (Step 6), and steady load (Step 7), as shown in Figs. 15 and 16. In these figures, the 0° position corresponds to the crown of the tunnel cross-section, with the angle increases in a counter-clockwise. Therefore, the 90° position represents the left waist of the tunnel, and 180° corresponds to the bottom of the shield tunnel.

Analysing the radial displacement of R6 (Fig. 15) reveals a gradual increase in displacement as the load type changes. Under the jack thrust force, the radial displacement is relatively uniform and positive. Under shield brush pressure, the segment experiences negative radial displacement, indicating an inward contraction. The deformation of R6 becomes more uniform during this phase, and radial displacement turns positive at the waist under the grouting pressure. However, the radial displacement of the crown and bottom decreases slightly, and the segment's deformation is no longer uniform and is further enhanced under ground loads and stable loads. Because circumferential bolts connect the adjacent segments, the joints open under the load; thus, the radial displacement of the segment jumps at each joint.

The bending moment of R6 was analysed in Fig. 16. It should be noted that when the segment's external side is under tension the bending moment is defined as positive. The bending moment distribution is more uniform under the combined jack thrust and shield brush pressure. As the angle increases, the bending moment fluctuates within a small range, but the directions of the bending moment under these two loads are opposite due to the transition in R6's deformation from expansion to compression. Under the grouting pressure, the segment exhibits a positive bending moment at the waist, while the bending moment at the crown remains low. As ground loads and steady loads are applied, the bending moment increases. Notably, the bending moment at the bottom of tunnel becomes slightly larger than at the vault, due to the greater vertical reaction force P_2 compared to the horizontal force P_1.

The stress distribution of R6 under each individual load type was obtained, and the ellipticity of the ring at each load step was calculated, as shown in Fig. 17. The ellipticity reflects the deformation of the segment ring under a specific load type and is defined as the ratio of the difference between the major and minor axes of the elliptical ring to the design length [53–55], as shown in Eq. (9).

$$\rho = \frac{D_{\max} - D_{\min}}{D} \tag{9}$$

where ρ is the ellipticity of the shield tunnel ring, $D_{\max}$ is the maximum external diameter of the ring, $D_{\min}$ is the minimum external diameter of the ring, and D is the design diameter of the shield tunnel ring.

Under the action of the jack thrust, the stress distribution is relatively uniform, with significant stress concentrated at the joints. Additionally, there is an expansion trend observed on the side where the longitudinal bolt is absent, leading to uneven deformation in that region. Under the shield brush pressure, the stress level increases further. Since the shield brush pressure is uniformly distributed on the outer surface of the segment and directed toward the center, it counteracts the expansion trend caused by the jack thrust, causing the segment to contract inward. The maximum stress is concentrated at the bolt joint, reflecting the segment's increased compression in response to the brush pressure.

The stress level decreases under the grouting pressure, although the stress at the joint remains high. As ground load and steady load are applied, the overall stress level of the segment gradually increases. The ellipticity of the segment also progressively increases under each load and eventually reaches 0.097 %. An analysis of the entire construction process shows that the segment experiences the highest stress level under the wire brush pressure, with notable stress concentration. This occurs because the segment is subjected to both the shield brush pressure and the larger jack thrust force transferred from R7, leading to uneven deformation under these combined loads. In practice, concrete segments are often prone to cracking and spalling under the influence of jack thrust and shield brush pressure during tunnel construction [36,56].

4.2. *Influence of void position*

The cases with $\alpha = 18°$ and $l = 1.5$ m were selected to analyse the influence of the void position on the mechanical performance of

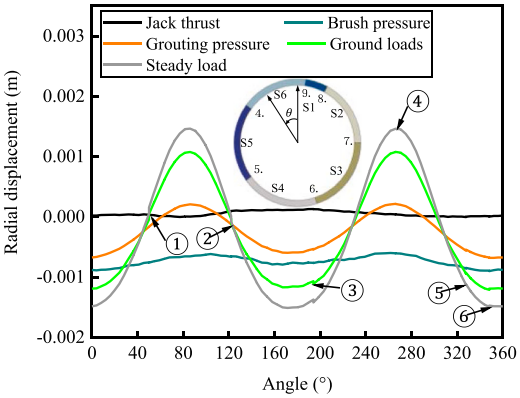

Fig. 15. Radial displacement of R6 subjected to individual load type.

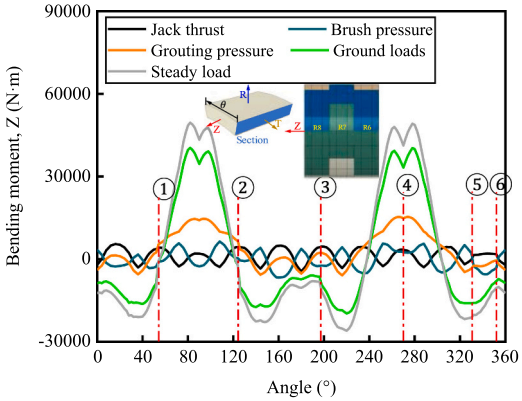

Fig. 16. Bending moment of R6 subjected to individual load type.

the segment (Cases 1 and 6). The displacement and bending moment of the segment under grouting pressure, ground pressure, and stable load were obtained and are further compared with the results of Case 1 (without voids).

The radial displacement and bending moment of R6, when the void is located at the crown, are shown in Figs. 18 and 19, respectively. An analysis of the radial displacement of R6 shows that the displacement at the crown is negative under the loads (inward contraction of tunnel ring). This deformation increases progressively as the loading continues. The final radial displacement at the crown, under the influence of voids, is smaller than that without voids because the voids prevent the direct transfer of ground pressure to the segment. As a result, the crown displacement is primarily influenced by the segments in the adjacent denser areas. Analysis of the segment's bending moment shows that it is positive under the applied loads, implying the outside side of the segment is tensioned while the inside is compressed, and the bending moment decreases gradually. Under normal conditions, the bending moment at the crown is negative; therefore, the void leads to a reversal of the bending moment, and the bending moment is larger compared to the case without a void, indicating a significant change in the structural behavior due to the void's influence. As the distance from the center of the void increases, the bending moment gradually decreases, reaching zero at the boundary of the void, and then becomes negative. This abrupt change in the direction of the bending moment makes the segment more prone to damage. Additionally, the impact of the void on the bending moment extends beyond the 18° range, affecting the segment's bending moment within a 45° range on both sides of the crown. This broader influence exacerbates the risk of structural stress and potential damage.

The radial displacement and bending moment of R6, when the void is located at the waist, are shown in Figs. 20 and 21, respectively. An analysis of the radial displacement of R6 shows that, under the applied loads, the displacement is positive, and the deformation gradually increases. Compared with the normal condition, the radial displacement of the segment with a void, caused by ground pressure, is larger. The void influences the radial displacement of the segment within a 50° range on both sides of the waist. As the distance from the void increases, the effect diminishes, and the radial displacement gradually aligns with that of the normal condition.

An analysing of the bending moment of the segment shows that, under the applied loads, the bending moment increases gradually and remains positive throughout. Compared with the normal condition, voids lead to a significant increase in the bending moment. Under grouting pressure, the bending moment exceeds that of the normal condition. Under grouting pressure, the bending moment exceeds that of the normal condition. The void affects the segment's bending moment across the range of 0° to 180°, causing notable changes. In the areas adjacent to the void, the bending moment decreases, highlighting the void's impact on the overall structural behavior.

4.3. *Influence of void angle*

The simulation results for cases with $l = 1.5$ m were selected to analyse the influence of the void angle on the mechanical state of the segment (Cases 1, 2, 5, 6, 7, and 10).

The radial displacement of R6 with different α was analysed, as shown in Figs. 22 and 23. When the void is located at the crown, the radial displacement is negative for all α values (that is, segment inward contraction). The contraction value gradually decreases with the increasing angle α. In addition, the void at the crown also impacts the segment at the waist, where the radial displacement is positive indicating a tendency for the segment to expand outward. However, this expansion gradually decreases as α α. The zero point of the radial displacement (where the displacement transitions from negative to positive) moves closer to the waist as α increases, indicating a shift in the deformation pattern with larger void angles.

When the void is located at the waist, the radial displacement at the waist remains positive for all values of α, and the displacement increases gradually as α increase. Additionally, the void at the waist affects the adjacent segments, but the zero point of the radial displacement remains unchanged, indicating that the primary impact of the void is localized around the waist without significantly altering the overall deformation pattern of the segment.

The different radial displacement trends observed when the void is located at the crown versus the waist are primarily due to the

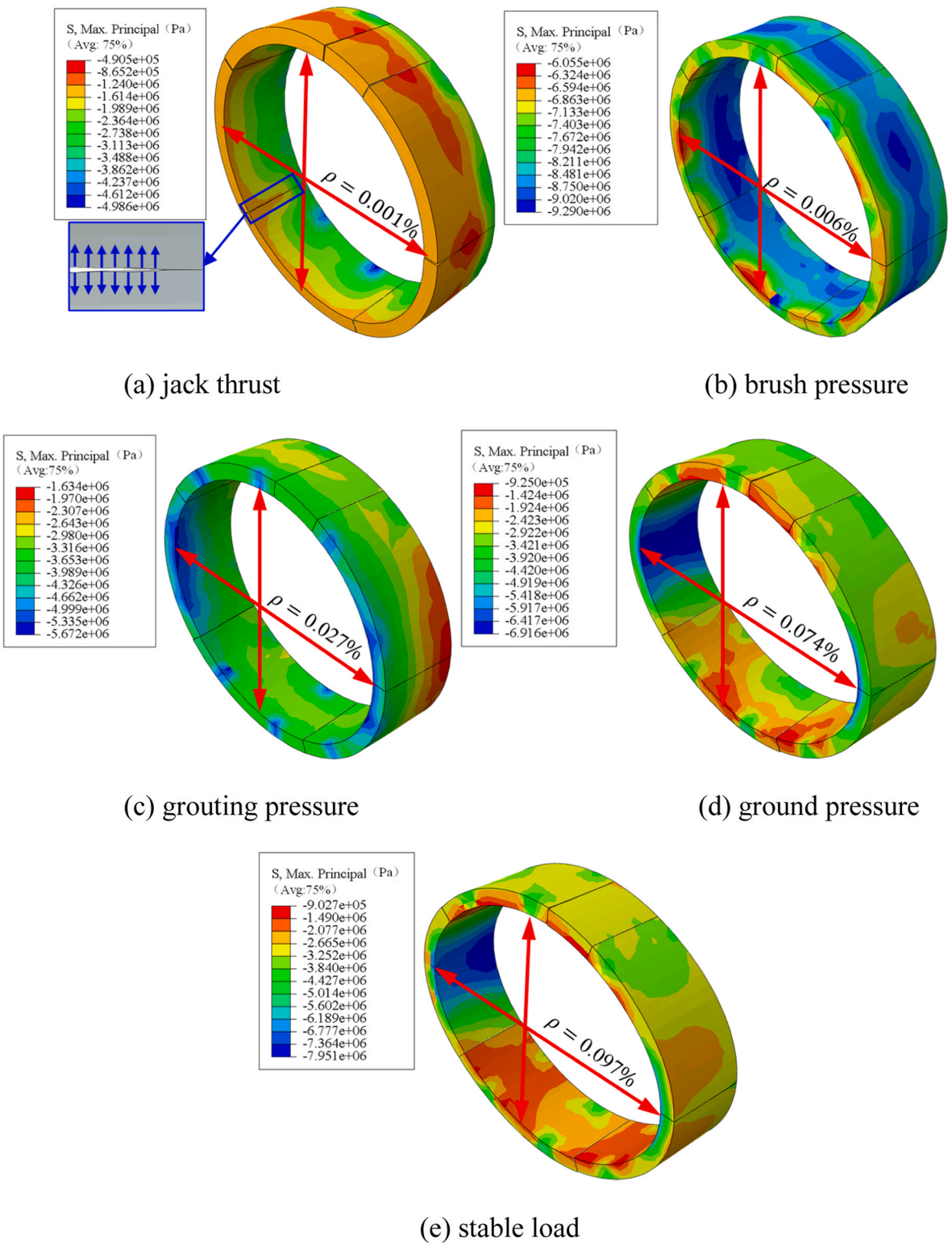

Fig. 17. Stress distribution of R6 under individual load type.

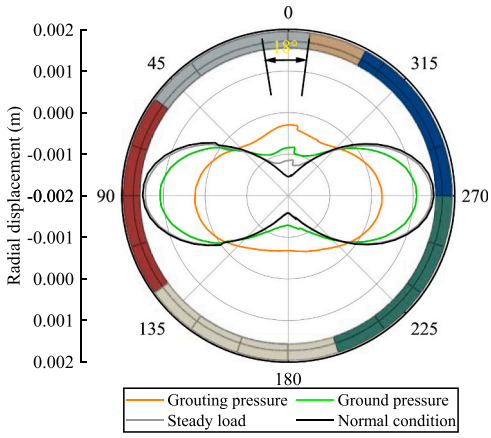

Fig. 18. Radial displacement of R6 when the void is located at the crown.

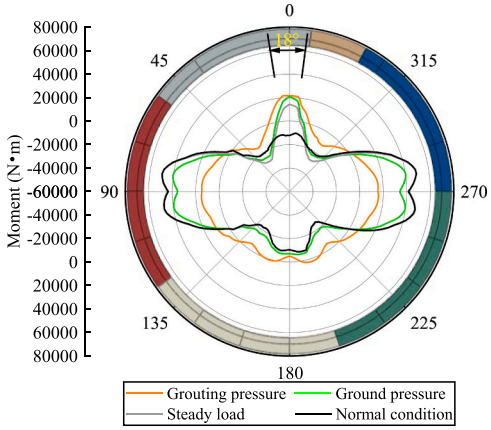

Fig. 19. Moment of R6 when the void is located at the crown.

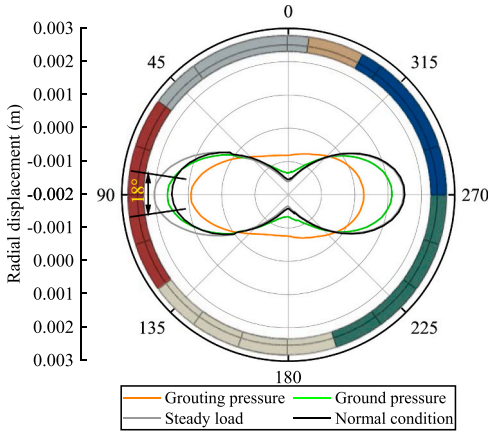

Fig. 20. Radial displacement of R6 when the void is located at the crown.

varying constraints exerted by the surrounding stratum on the segment. In a shield tunnel, the vertical load from the stratum aligns with the direction of the principal stress, and the crown directly bears this ground pressure. When a void is present at the crown, the ground pressure cannot be transferred directly to the segment, leading to a situation where the deformation of the segment in the void area is mainly governed by the adjacent dense areas. This reduces the radial displacement of the segment at the crown. At the waist, the

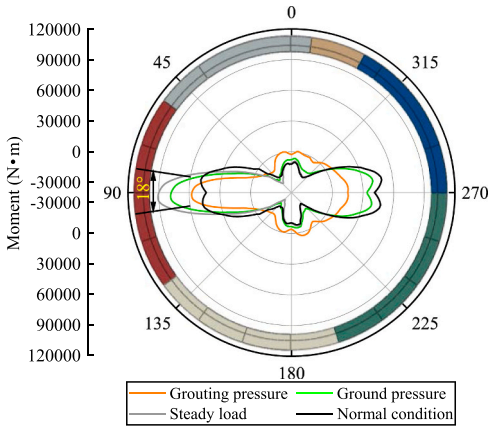

Fig. 21. Moment of R6 when the void is located at the waist.

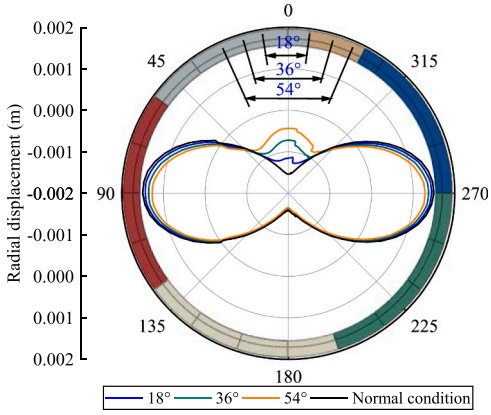

Fig. 22. Radial displacement of the crown with different α.

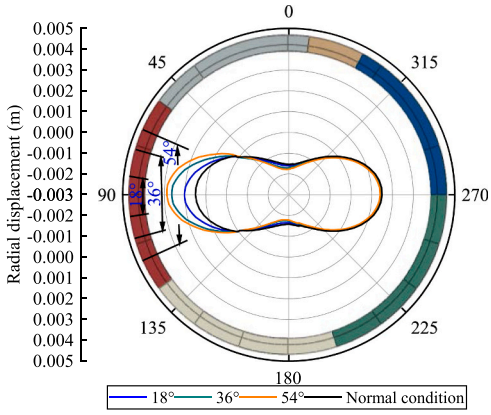

Fig. 23. Radial displacement of the waist with different α.

segment exhibits an expansion trend due to the principal stress, and the ground pressure typically acts to restrain this deformation, counteracting the expansion. When a void is present at the waist, the stratum is unable to exert this restraining force, leading to increased radial displacement as the segment expands without sufficient resistance from the surrounding ground.

The bending moment of R6 with different values of α was analysed, as shown in Figs. 24 and 25. The existence of voids increases the bending moment of segments at both the crown and waist. When α is 18° and 36°, the bending moment increases gradually. However, when $\alpha = 54°$, the bending moment is close to that when $\alpha = 36°$, and it decreases slightly at the centre of the void. In other words, the

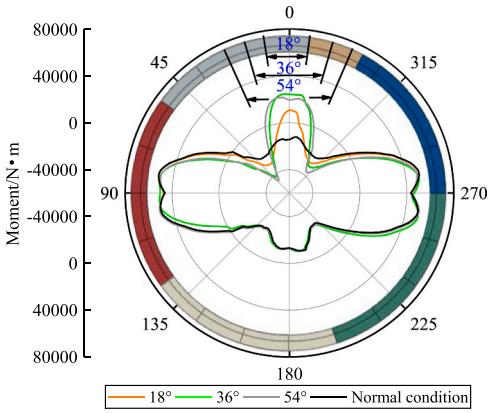

Fig. 24. Moment of the crown with different α.

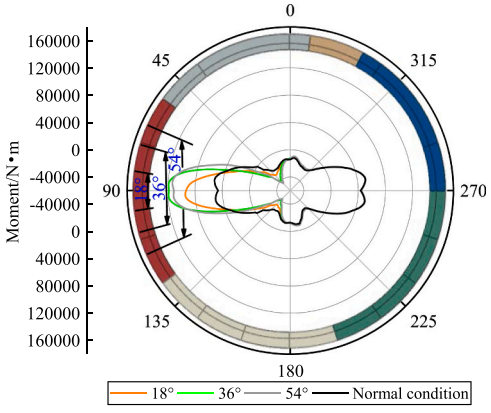

Fig. 25. Moment of the waist with different α.

change in bending moment is not completely positively correlated with the void angle, and when the void reaches a certain angle, the segment bending moment no longer changes. The difference is that when the void is located at the crown, it reverses the bending moment, whereas the bending moment at the waist is always positive.

The radial displacements of the crown and waist of R1–R13 were analysed, as shown in Fig. 26. The void affects the radial displacement of R6 and that of the adjacent ring. The crown void reduces the radial contraction of the adjacent ring, while the vault void intensifies the radial expansion of the adjacent ring. Segment that are closer to R6 are more affected, and the void angle positively correlates with the degree of influence. For the rings behind R6 (R1 to R5), the influence of the void also grows as the void angle

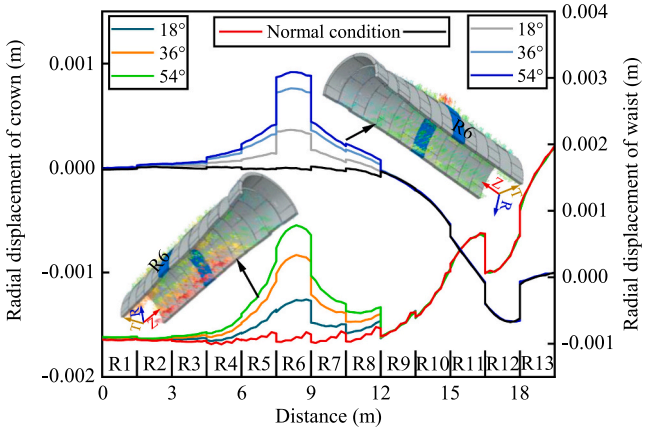

Fig. 26. Radial displacement of R1–R13 with different α.

increases; however, this effect becomes negligible for R3 and beyond, indicating a diminishing impact as the distance from R6 increases.

For the rings in front of R6, specifically R7 to R13, the influence of the void is eliminated in R9. This is because R11 to R13 are subjected to grouting pressure, shield brush pressure, and jack thrust, respectively. As these three rings are progressively loaded, the deformation of the segments becomes primarily governed by these three loads. Consequently, the void's impact on segment deformation is mainly limited to the three rings behind (R3 to R5) and the two rings in front of R6 (R7 and R8). This localized influence alters the longitudinal curvature of the shield tunnel, causing misalignment or dislocation between adjacent rings. In weaker strata, such as muddy soil layers, this tendency for negative dislocation may be further amplified, increasing the risk of deformation and structural instability.

4.4. Influence of void length

The cases with $l = 1.5$ m (affecting R6), 3.0 m (affecting R6 & R7), and 4.5 m (affecting R6 & R7 & R8) were selected to analyse the influence of void length on the deformation and mechanical properties of segments. These cases were examined with $\alpha = 36°$, with the voids located at the crown and waist (Cases 2–4 and 7–9).

The radial displacement and bending moment of R6 with different l when the void was located at the crown were obtained, as shown in Figs. 27 and 28, respectively. As l increase, the radial displacement at the crown gradually shifts from negative to zero. Simultaneously, the range of the void's influence on the adjacent dense area also expands. At the same time, the radial expansion at the waist of the segment decreases as the void length increases. Analysing the distribution of the bending moment shows that the void changes the bending moment from negative to positive, and the bending moment of the crown increases gradually with increasing.

However, the relationship between l and the bending moment is not linear. When l increases from 1.5 to 3.0 m, the bending moment at the crown increases from 24,020 to 39,960 N • m (an increase of 15,940 N • m). When l further increases from 3.0 to 4.5 m, the bending moment only increases from 39,960 to 44,940 N • m (an increase of 4980 N • m). This indicates that the impact of increasing l on the segment's bending moment diminishes as the void boundary extends farther from R6, reducing the effect of changes in the bending moment at the void boundary on R6. Additionally, the negative bending moment in the adjacent dense area also increases with the increase in l, but this is also nonlinear. For example, at 45°, the bending moment for a void length of 3.0 m is 41230 N • m which is quite close to that for a void length of at 4.5 m (4400 N • m).

The vertical displacements of the crown with different l of R1 to R13 and the stress distribution of R6 to R8 were obtained, as shown in Fig. 29. As l increase, the vertical displacement increases gradually, and the void's influence extends to a larger area, affecting adjacent rings. For R1 to R5, the vertical displacement remains the same when l is 3.0 and 4.5 m, suggesting that the void's impact on the segment's displacement reaches a maximum when the void length is 4.5 m.

For the rings in front of R6 (R7 to R13), the void mainly affects the displacement of the segment within the range of the front two rings. Unlike the continuous deformation of the rings after R6, the displacement of the segment suddenly increases negatively at the edge of the void, and this phenomenon is closer to the loading end. Therefore, the closer the void is to the segment under the construction load, the more likely it is to cause geometrical dislocation. Analysing the stress field distribution of R6 to R8 reveals that, as l increase, the deformation of the segment also gradually increases, with the joint openings becomes more obvious. At the same time, there is a significant stress concentration in the void area. s l increases, the range of the stress concentration, mainly at the centre of the void, also gradually increases, which can potentially damage the segment during the construction stage.

The results for the scenario where the void is located at the waist are shown in Figs. 30 and 31. The simulation shows that the radial displacement increases as l increasing. In terms of bending moment distribution, the moment at the waist is larger than that in the normal condition, with the maximum bending moment occurring when $l = 1.5$ m (where the void is only located in R6). The bending moment at the waist is close when $l = 3.0$ and4.5m, which can be attributed to the fact that the segment joints (S5 and S6) at the waist in R7 influence the bending behaviour. At the centre of the void, the increase in the bending moment is transferred to the joint bolts,

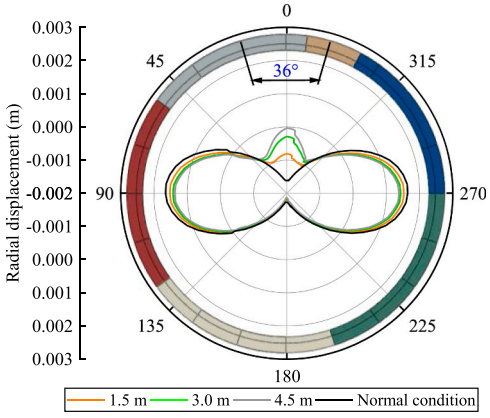

Fig. 27. Radial displacement of tunnel ring when the void located at the crown with different l.

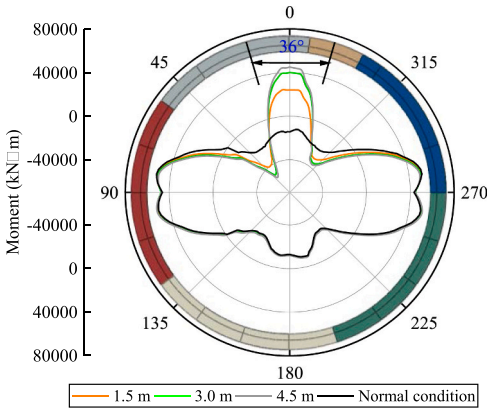

Fig. 28. Moment of tunnel ring when the void located at the crown with different *l*.

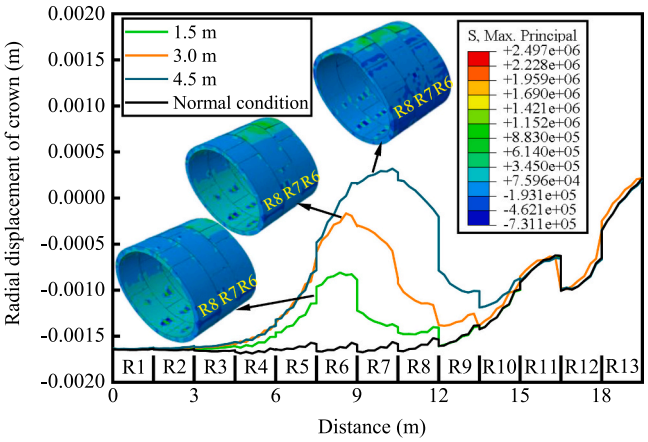

Fig. 29. Vertical displacement of the crown of R1 toR13 with different *l*.

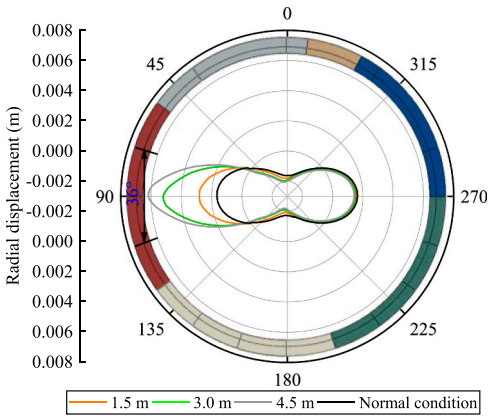

Fig. 30. Radial displacement of tunnel ring when the void located at the waist with different *l*.

leading to joint opening and releasing part of the bending moment. This joint opening reduces the buildup of moment, explaining the similar values for larger void lengths.

The horizontal displacement of the segment at the waist is shown in Fig. 32, along with the stiffness degradation rate (SDEG) of the concrete segment, which characterise the degree of segment damage [46]. As *l* increase, the horizontal displacement increases gradually, and the influence the void on the adjacent rings expands. The maximum radial displacement consistently occurs at the center of the void. An analysis of the stiffness degradation of the segment shows that the damage degree of the segment increases with

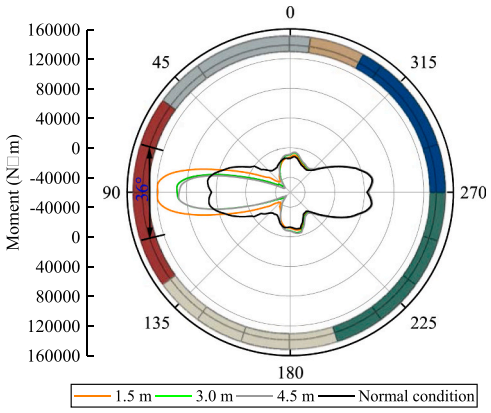

Fig. 31. Moment of tunnel ring when the void located at the waist with different *l*.

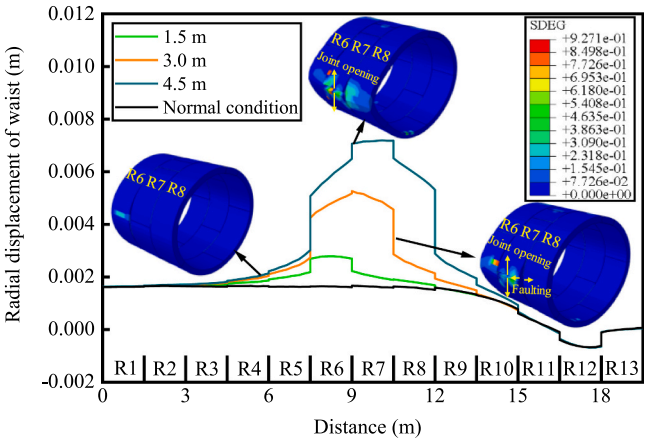

Fig. 32. Radial displacement of the waist of R1 toR13 with different void lengths.

the increase in *l*. R7 is a special ring in which the joints are located at the centre of the void, making it more vulnerable to deformation and stress concentration, which further accelerates the damage process. The opening of the R7 joint also gradually increases from 1.5 mm ($l = 3.0$ m) to 3.0 mm ($l = 4.5$ m). This joint opening results in an increase in bolt stress, which in turn reduces the bending moment of the segment. At the same time, the dislocation deformation between R7 and R8 is highlighted when $l = 3.0$ m, but when $l = 4.5$ m, the radial displacement of R8 begins to increase, and the dislocation is no longer obvious. Therefore, when the void is located at the joint of the segment, the opening of the segment joint can mitigate the increase in bending moment; however, it also causes an increase in bolt stress, and notably, excessive bolt stress can potentially lead to tensile failure of the surrounding concrete.

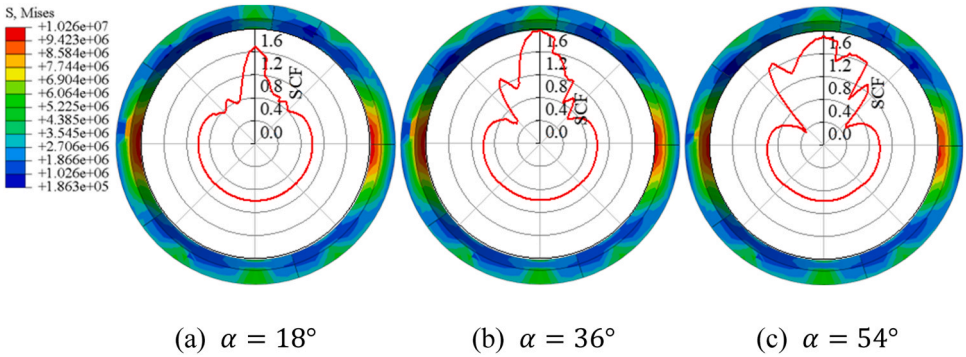

Fig. 33. SCF of R6 when the void is located at the crown.

4.5. Stress concentration factor analysis

The stress concentration factor (SCF) reflects the change in the stress state of a concrete segment caused by void defects. A higher stress concentration factor usually indicates that the segment has a greater risk of failure in this part, and the SCF can be calculated using Eq. (10).

$$SCF = \frac{\sigma_{void}}{\sigma_{normal}} \tag{10}$$

where SCF is the stress concentration factor of the segments, σ_{void} is the stress of the segments under the influence of voids and σ_{normal} is the stress of the segments without voids. If SCF exceed 1.0, stress concentration occurs in this part because of the void. If SCF lower 1.0, the stress of the segment decreases compared with the normal condition. If $SCF = 1.0$, the stress state of the segment does not change.

The segment stress results of scenarios where the void located at the crown were analysed, as shown in Fig. 33. The maximum SCF appears at the centre of the void, but the relationship between the maximum SCF and α is not linear. The maximum SCF (2.0) was observed when $\alpha = 36°$, followed by $\alpha = 54°$ with a SCF of 1.9, and finally $\alpha = 18°$ with a SCF of 1.7. As α increase, the range of the segment experiencing stress concentration expands, extending beyond the void area and into the adjacent dense regions. This broader range of stress concentration makes segments near the voids more susceptible to damage, while the stress in segments farther from the voids tends to decrease slightly. Additionally, the SCF at the joint often drops suddenly, especially when $\alpha = 54°$. This occurs because the stress concentration at the joint can be alleviated by the greater deformation capacity of the bolt spring, which helps release the stress.

The segment stress results of scenarios where the voids are located at the waist are shown in Fig. 34. The maximum SCF appears at the centre of the void (at 90°), and the range of stress concentration expands as α increases. Notably, the SCF curve is symmetrically distributed with respected to the horizontal axis extending through the void's center. However, when $\alpha = 54°$, the SCF in the adjacent segment S6 is 1.22, which is higher than the SCF of 1.01 in the standard segment S4. This difference is due to the varying ground pressures exerted on the two segments.

The stress distribution of the segment under different values of l is shown in Figs. 35 and 36. For the scenarios where the void is located at the crown (Fig. 35), changes in l do not significantly affect the stress distribution in the segment. The maximum SCF always appears at the centre of the void and an increase in l usually correspond to a higher SCF value. Specifically, the SCF reaches 2.0, 2.28, and 2.44 for $l = 1.5$, 3.0 and 4.5 m, respectively. For the scenario where the void located at the waist (Fig. 36), change in l also leads to a significant change in the distribution form of the SCF. Unlike the case when $l = 1.5$ m, the maximum SCF for $l = 3.0$ and $l = 4.5$ m no longer appears in the void center but at 45° on both sides. This shift is due to the location of the joints in R7 being at the center of the void. The reduced stiffness at joint R7 allows the bending moment to transfer to R6, causing the stress concentration to shift away from the void's center and redistribute along the adjacent segments.

Overall, the presence of grouting voids leads to stress redistribution in the concrete segments. In the most adverse scenario, the stress in the segment was increased by as high as two times compared to the normal case (Fig. 33(b)), indicating that voids in the crown segment significantly heighten the risk of damage to the concrete structure. In addition, the existence of voids increased the tendency of outward bending of the segment, and the increase in the tensile stress caused by the void was mainly concentrated in the outer surface of the segment, which means that the outer side of the segment is more prone to tensile damage, and hence deteriorating the long-term serviceability of the tunnel lining.

4.6. Discussion and limitations

In practical scenarios, engineers cannot directly observe grouting voids, but segment damage and large deformations caused by these void pose significant threats to the safety of shield tunnels. The 3D numerical simulation demonstrates that grouting voids have significant negative impacts on the concrete segments with the severity of the effect closely correlated to the void's location, angle, and length. The presence of voids alters the deformation pattern of the concrete segments. The void at the crown reduces the inward

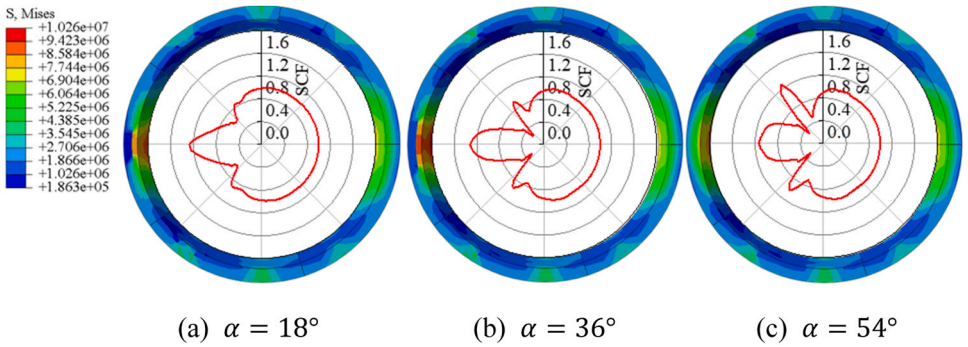

Fig. 34. SCF of R6 when the void is located at the waist.

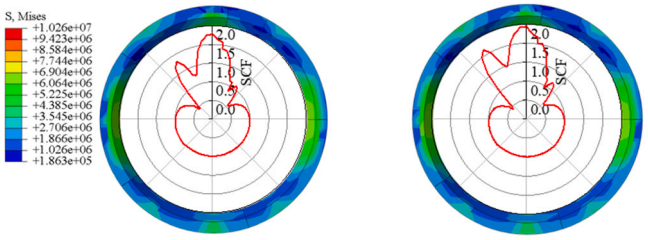

(a) $l = 3.0$ m **(b)** $l = 4.5$ m

Fig. 35. SCF of R6 when the void is located at the crown.

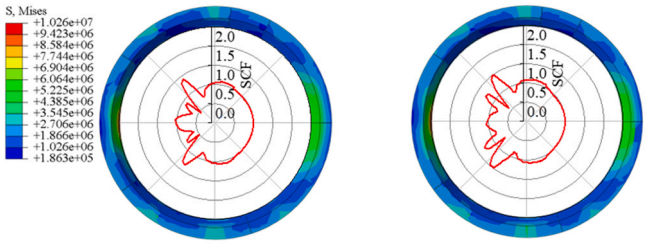

(a) $l = 3.0$ m **(b)** $l = 4.5$ m

Fig. 36. SCF of R6 when the void is located at the waist.

contraction of the tunnel ring, while the voids at the waist intensify the outward expansion. An excessive void angle alters the force state of the segment. The most notable impact is that voids in the crown cause a reversal of the bending moments, potentially leading to tensile damage due to the imbalance of forces. The effect of void length decreases gradually, and when the length of the void is greater than 3.5 m, it no longer significantly increases the segment's bending moment.

In addition, the effect of the void is not only limited to the close segment where the void is located but will also lead to stress state changes in the adjacent segments. For example, the analysis shows that the most serious stress concentration occurs at 45° on both sides of the void. Therefore, in the actual shield tunnel, the influence area of grouting void defects may extend beyond the void location. This may imply that when detecting and handling the void defects, the segments of concern to be monitored and checked should expand to the wider range.

However, this study still has some limitations. Firstly, the simplifications in modelling the tunnel structure can be further refined. The use of a bolt spring with equivalent stiffness to represent the actual bolt's behavior does not account for specific details, such as hand holes and the falcon structure. This simplification may introduce bias into the stress analysis. A more accurate geometric model is needed to simulate the condition of the contact surfaces. Preferably, change of joint stiffness, for instance the alternative joint configurations or variations in bolt stiffness, may affect the area of stress redistribution, and therefore an exploration on this issue is also suggested. Secondly, the shield tunnel is considered in an idealized state, and the joint dislocation and ring misalignments caused by construction errors have not been considered in this study. The coupling effect of construction errors and grouting voids can be considered in further studies, and this coupling effect may lead to changes in the deformation pattern of shield tunnels.

Furthermore, this study only investigates the scenario where void exists and extends on a maximum of 3 consecutive rings. The trends observed in stress redistribution and deformation behavior are primarily driven by localized effects and are expected to remain consistent for longer tunnel sections. However, in a more realistic scenario, multiple voids may present behind the tunnel lining at discrete locations longitudinally, and the spatial effects between adjacent voids could lead to more complex stress states in the segments. In that case longer shield tunnel modeling is needed to capture the spatial effects of multiple voids.

In addition, accurately simulating the time-dependent behavior of grouting material is a challenging task. In this study, the reduction in grouting pressure was used to reflect the curing process of the grout. While the applicability of this method in numerical simulations of the shield tunnel excavation process has been validated, the simplified simulation method does not capture the time-dependent behavior of the strength variation in the grouting material, which may have an impact on the redistribution of stresses in the tunnel lining. Further study requires higher-precision numerical models to reflect the formation progress of voids due to grouting error.

5. Conclusions

In shield tunnel construction, grouting void defects can significantly affect the structural safety of the tunnel lining. To address this issue, the current study develops a 3D finite-element model of a shield tunnel using the load-structure method, specifically investigating the impact of grouting void defects on the mechanical behavior of concrete segments. The simulation model incorporates

various void characteristics, such as position, angle, and length, to assess their influence on segment stress and deformation. The deformation of the tunnel ring, bending moments, and stress concentrations were analysed and compared. From these analyses, the following conclusions are drawn:

(1) The presence of voids prevents ground pressure from being directly transferred to the segments, leading to changes in both the radial displacement and bending moment distribution of the tunnel ring. A void at the crown leads to inward contraction of the tunnel ring, while a void at the waist result in outward expansion. The void causes an increase in the segment's bending moment, with the magnitude of this increase being positively correlated with the void angle. Voids at the crown also reverse bending moments, with an increase of approximately 24 kN·m compared to the normal case.

(2) The extent of the influence exerted by grouting voids on the segments expands as the void angle increases. Longer voids (4.5 m) amplify bending moments by up to 15 % compared to shorter voids (1.5 m). Similarly, voids with larger angles (54°) expand the affected region and further elevate stress levels.

(3) Voids not only affect the segment directly beneath them but also propagate stress and deformation changes to adjacent rings, up to three rings away. This highlights the broader structural implications of grouting defects.

(4) The presence of voids results in a stress concentration factor (SCF) increase of up to 2.44, with the highest SCF observed at the center of voids. The range of stress concentration extends to approximately 45° on either side of the void, highlighting the potential for damage in adjacent segments. Additionally, stress concentration at the joint is usually lower than in the concrete section, as excessive bolt deformation helps to relieve the stress.

The findings of this study contribute to quantifying the deformation of segments affected by invisible voids, which may aid in recognizing structural damage in shield tunnels. However, due to the costs associated with numerical simulations and the complexity of the factors considered, the current modeling approach has some limitations. Therefore, future work should focus on developing a more refined numerical model that better accounts for the accurate formation of joint interfaces and the effects of variable ground conditions.

CRediT authorship contribution statement

Chen Xiangsheng: Resources, Methodology, Funding acquisition. **Dang Pengliang:** Writing – review & editing, Supervision. **Zhang Xuehui:** Writing – review & editing, Writing – original draft, Software, Data curation. **Shen Jun:** Writing – review & editing, Software, Data curation, Conceptualization. **Bao Xiaohua:** Writing – review & editing, Methodology, Funding acquisition. **Wu Xianlong:** Writing – review & editing, Writing – original draft, Software, Methodology, Formal analysis. **Cui Hongzhi:** Writing – review & editing, Supervision, Methodology, Funding acquisition.

Declaration of Competing Interest

The authors declare that they have no known competing financial interests or personal relationships that could have appeared to influence the work reported in this paper.

Acknowledgements

This study is supported by the National Natural Science Foundation of China (No. 52379104 & 52090084), the Shenzhen Science and Technology Program (No. KQTD20200909113951005 & 20231121224122001).

Appendix

The tunnel was buried at a depth of 20 m, which is more than twice the outer diameter of the tunnel. In accordance with the Chinese code (GB/T 51438–2021), the unloading arch effect of the soil was considered. The ground loads of each segments was calculated using Terzaghi's relaxation ground pressure theory, as shown in Fig. A1.

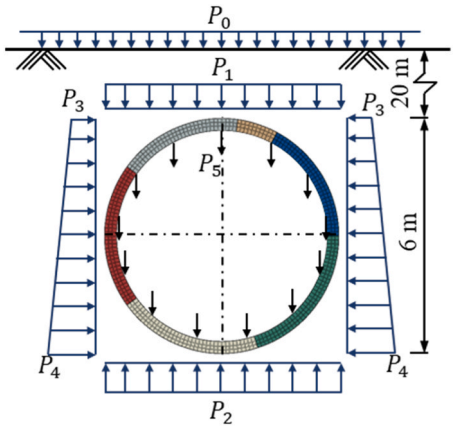

Fig. A1. Distribution of ground pressure on segments

Half the loose range of soil is

$$B_1 = B_0 \cot\left(\frac{\pi}{8} + \frac{\varphi}{4}\right) \tag{1}$$

where B_1 is half the loose range of the soil, R is the outer radius of the shield tunnel, and φ is the internal friction angle of the soil.

The loosening height of the soil is

$$h_0 = \frac{R\left(1 - \frac{c}{B_1 \gamma}\right)}{K_0 \tan\varphi}\left(1 - e^{-K_0 \tan\varphi \frac{H}{B_1}}\right) + \frac{P_0}{\gamma} e^{-K_0 \tan\varphi \frac{H}{B_1}} \tag{2}$$

where K_0 is the ratio of horizontal soil pressure to vertical soil pressure, c is the cohesion force of the soil, γ is the weight of the soil, H is the thickness of the overlying soil, and P_0 is the overload on the ground, which is 20 kPa.

It was calculated that $B_1 = 6.1$ m, $h_0 = 17.07$ m, and the ground pressure of each part was

$$P_1 = h_0 \gamma = 351.642\text{kPa} \tag{3}$$

$$P_2 = P_1 + P_5 = 366\text{kPa} \tag{4}$$

$$P_3 = \lambda P_1 = 140.8\text{kPa} \tag{5}$$

$$P_4 = \lambda(P_1 + \gamma B_0) = 190.3\text{kPa} \tag{6}$$

Data Availability

Data will be made available on request.

References

[1] X.D. Bai, W.C. Cheng, G. Li, A comparative study of different machine learning algorithms in predicting EPB shield behaviour: a case study at the Xi'an metro, China, Acta Geotech. 16 (12) (2021) 4061–4080, https://doi.org/10.1007/S11440-021-01383-7.
[2] S. He, J. Lai, Y. Li, K. Wang, L. Wang, W. Zhang, Pile group response induced by adjacent shield tunnelling in clay: scale model test and numerical simulation, Tunn. Undergr. Space Technol. 120 (2022) 104039, https://doi.org/10.1016/J.TUST.2021.104039.
[3] X. Jiang, X. Zhang, X. Zhang, L. Long, Y. Bai, B. Huang, Advancing shallow tunnel construction in soft ground: the pipe-umbrella box jacking method, Transp. Res. Rec. 2678 (9) (2023) 150–168, https://doi.org/10.1177/03611981231225430.
[4] D. Xu, X. Zhang, W. Chen, X. Jiang, Z. Liu, Y. Bai, Utilisation of the deep underground space in Shanghai, Proc. Inst. Civ. Eng.: Munic. Eng. 172 (4) (2019) 218–223, https://doi.org/10.1680/jmuen.18.00029.
[5] X. Guo, P. Geng, Z. Xu, R. Tang, C. He, Q. Cai, Longitudinal seismic response of a shield tunnel considering longitudinal bolt prestress under transverse excitation, Int. J. Geomech. 24 (3) (2024) 04024011, https://doi.org/10.1061/IJGNAI.GMENG-8537.
[6] Y. Shen, J. Ling, W. Wang, H. Zhu, Z. Yan, 3D numerical investigation on response of shield tunnel under combined effects of fire and structural loading, Tunn. Undergr. Space Technol. 128 (2022) 104659, https://doi.org/10.1016/j.tust.2022.104659.
[7] Y. Shen, H. Zhu, Z. Yan, L. Zhou, T. Zhang, Y. Men, Y. Lu, Thermo-mechanical analysis of fire effects on the structural performance of shield tunnels, Tunn. Undergr. Space Technol. 132 (2023) 104885, https://doi.org/10.1016/j.tust.2022.104885.

[8] Z. Yan, J. Li, Y. Shen, Z. Xiao, Q. Ai, H. Zhu, Damage identification method on shield tunnel based on PLSR and equivalent damage analysis, Tunn. Undergr. Space, Technol. 137 (2023) 105127, https://doi.org/10.1016/j.tust.2023.105127.
[9] D.M. Zhang, S. Chen, R.C. Wang, D.M. Zhang, B.J. Li, Behaviour of a large-diameter shield tunnel through multi-layered strata, Tunn. Undergr. Space Technol. 116 (2021) 104062, https://doi.org/10.1016/J.TUST.2021.104062.
[10] H. Jin, J. Su, C. Zhao, Relationship between invert-filling disengaging and deformation of shield tunnel using staggered assembled segment, KSCE J. Civ. Eng. 26 (4) (2022) 1966–1977, https://doi.org/10.1007/S12205-022-1414-5.
[11] X.S. Chen, J. Shen, X.H. Bao, X.L. Wu, W.C. Tang, H.Z. Cui, A review of seismic resilience of shield tunnels, Tunn. Undergr. Space Technol. 136 (2023) 105075, https://doi.org/10.1016/J.TUST.2023.105075.
[12] W. Yang, J. Zheng, R. Zhang, S. Liu, W. Zhang, Dynamic prediction of over-excavation gap due to posture adjustment of shield machine in soft soil, Undergr. Space 16 (2024) 44–58, https://doi.org/10.1016/j.undsp.2023.09.004.
[13] X. Jiang, H. Zhu, Z. Yan, F. Zhang, F. Ye, P. Li, X. Zhang, Z. Dai, Y. Bai, B. Huang, A state-of-art review on development and progress of backfill grouting materials for shield tunneling, Dev. Built Environ. 16 (2023) 100250, https://doi.org/10.1016/j.dibe.2023.100250.
[14] S. He, J. Lai, L. Wang, K. Wang, A literature review on properties and applications of grouts for shield tunnel, Constr. Build. Mater. 239 (2020) 117782, https://doi.org/10.1016/j.conbuildmat.2019.117782.
[15] K. Kasper, B. Meschke, A numerical study of the effect of soil and grout material properties and cover depth in shield tunnelling, Comput. Geotech. 33 (4-5) (2006) 234–247, https://doi.org/10.1016/j.compgeo.2006.04.004.
[16] S. Wang, C. He, L. Nie, G. Zhang, Study on the long-term performance of cement-sodium silicate grout and its impact on segment lining structure in synchronous backfill grouting of shield tunnels, Tunn. Undergr. Space Technol. 92 (2019) 103015, https://doi.org/10.1016/j.tust.2019.103015.
[17] R.P. Chen, P. Zhang, X. Kang, Z.Q. Zhong, Y. Liu, H.N. Wu, Prediction of maximum surface settlement caused by earth pressure balance (EPB) shield tunneling with ANN methods, Soils Found. 59 (2) (2019) 284–295, https://doi.org/10.1016/j.sandf.2018.11.005.
[18] S. He, J. Lai, L. Wang, K. Wang, A literature review on properties and applications of grouts for shield tunnel, Appl. Mech. Mater. 239 (2020) 117782, https://doi.org/10.1016/j.conbuildmat.
[19] J. Shi, F. Wang, D. Zhang, W. Huang, Refined 3D modelling of spatial-temporal distribution of excess pore water pressure induced by large diameter slurry shield tunneling, Comput. Geotech. 137 (2021) 104312, https://doi.org/10.1016/j.compgeo.2021.104312.
[20] J.X. Zhang, N. Zhang, A. Zhou, S.L. Shen, Numerical evaluation of segmental tunnel lining with voids in outside backfill, Under Space 7 (5) (2022) 786–797, https://doi.org/10.1016/J.UNDSP, 2021.12.007.
[21] L. Wan, X. Xie, L. Wang, P. Li, H. Yin, Cavity location method for operational metro tunnels based on perturbation theory, KSCE J. Civ. Eng. 25 (6) (2021) 2300–2313, https://doi.org/10.1007/S12205-021-1691-4.
[22] Z.S. Wu, H.H. Zhao, H.Q. Xie, Y.C. Dong, L. Fang, M.N. Wang, Y. Liu, Distribution characteristics of pea gravel behind segment in shield tunnel boring machine tunnels, Adv. Eng. Sci. 10 (1) (2023) 1–12, https://doi.org/10.15961/j.jsuese.202201182.
[23] Z.S. Wu, H.H. Zhao, H.Q. Xie, Y.C. Dong, L. Fang, M.N. Wang, Y. Liu, Distribution characteristics of pea gravel behind segment in shield tunnel boring machine tunnels, Adv. Eng. Sci. 10 (1) (2023) 1–12, https://doi.org/10.15961/j.jsuese.202201182.
[24] Z.S. Wu, H.H. Zhao, H.Q. Xie, Y.C. Dong, L. Fang, M.N. Wang, Y. Liu, Distribution characteristics of pea gravel behind segment in shield tunnel boring machine tunnels, Adv. Eng. Sci. 10 (1) (2023) 1–12, https://doi.org/10.15961/j.jsuese.202201182.
[25] D. Liu, F. Wang, F. Hu, H. Huang, J. Zuo, C. Tian, D. Zhang, Structural responses and treatments of shield tunnel due to leakage: a case study, Tunn. Undergr. Space Technol. 103 (2020) 103471, https://doi.org/10.1016/j.tust.2020.103471.
[26] L. He, F. Deng, P. Jia, Causes and treatment measures of sudden segment damage failures in a shield tunnel under construction, Mod. Tunn. Technol. 59 (1) (2022) 225–231, https://doi.org/10.13807/j.cnki.mtt.2022.01.026.
[27] C. Leung, M.A. Ma, An experimental study of the effect of local contact loss on the earth pressure distribution on existing tunnel linings, Tunn. Undergr. Space Technol. 26 (1) (2011) 139–145, https://doi.org/10.1016/j.tust.2010.08.003.
[28] X. Qin, G. Zhang, R. Ge, Effect of erosion void on segmental tunnel lining: 2D numerical investigation, Transp. Geotech. 35 (2022) 100792, https://doi.org/10.1016/J.TRGEO.
[29] Y. Shi, Z. Chen, D. Wei, T. Zhang, X. Zhou, X. Zhao, J. Hu, Y. Zhou, Analysis of structural response of subway shield tunnel lining under the influence of cavities, Adv. Civ. Eng. J. 2021 (2021) 3326595, https://doi.org/10.1155/2021/3326595.
[30] N. Yasuda, K. Tsukada, T. Asakura, Elastic solutions for circular tunnel with void behind lining, Tunn. Undergr. Space Technol. 70 (2017) 274–285, https://doi.org/10.1016/j.tust.2017.08.032.
[31] N. Yasuda, K. Tsukada, T. Asakura, Three-dimensional seismic response of a cylindrical tunnel with voids behind the lining, Tunn. Undergr. Space Technol. 84 (2019) 399–412, https://doi.org/10.1016/j.tust.2018.11.026.
[32] X. Qin, G. Zhang, R. Ge, Effect of erosion void on segmental tunnel lining: 2D numerical investigation, Transp. Geotech. 35 (2022) 100792, https://doi.org/10.1016/j.trgeo.2022.100792.
[33] B. Min, C. Zhang, X. Zhang, H. Wang, D. Zhang, Cracking performance of asymmetric double-arch tunnels due to the voids behind linings, Thin. Wall. Struct. 154 (2020) 106856, https://doi.org/10.1016/j.tws.2020.106856.
[34] C. Zhang, B. Min, H. Wang, S. Zhang, Mechanical properties of the tunnel structures with cracks around voids behind linings, Thin. Wall. Struct. 181 (2022) 110117, https://doi.org/10.1016/j.tws.2022.110117.
[35] C. Leung, M.A. Meguid, An experimental study of the effect of local contact loss on the earth pressure distribution on existing tunnel linings, Tunn. Undergr. Space Technol. 26 (1) (2011) 139–145, https://doi.org/10.1016/j.tust.2010.08.003.
[36] H. Jin, K. Yu, Q. Gong, S. Zhou, Load-carrying capability of shield tunnel damaged by shield shell squeezing action during construction, Thin-Walled Struct. 132 (2018) 69–78, https://doi.org/10.1016/j.tws.2018.07.057.
[37] P. Chaipanna, P. Jongpradist, 3D response analysis of a shield tunnel segmental lining during construction and a parametric study using the ground-spring model, Tunn. Undergr. Space Technol. 90 (2019) 369–382, https://doi.org/10.1016/j.tust.2019.05.015.
[38] S.M. Wang, Q.Y. Yu, B. Peng, X.F. He, J.B. Yao, Three-dimensional discontinuous contact model for shield tunnels with double-layer lining based on plastic-damage model, Chin. J. Rock. Mech. Eng. 35 (02) (2016) 303–311, https://doi.org/10.13722/j.cnki.jrme.2015.0158.
[39] GB/T 51438-2021, 2021. Standard for design of shield tunnel engineering. Beijing: China Architecture and Building Press.
[40] A.M. Wood, The circular tunnel in elastic ground, Géotechnique 25 (1) (1975) 115–127, https://doi.org/10.1680/geot.1975.25.1.115.
[41] Y. Koyoma, T. Nishimura, The design of lining segment of shield tunnel using a beam-spring model, Railw. Tech. Res. Inst., Q. Rep. 39 (1) (1998) 23–27.
[42] O. Arnau, C. Molins, Experimental and analytical study of the structural response of segmental tunnel linings based on an in situ loading test, Tunn. Undergr. Sp. Technol. 26 (6) (2011) 778–788, https://doi.org/10.1016/j.tust.2011.04.005.
[43] L.Z. Wang, Z. Wang, L.L. Li, J.C. Wang, Construction behavior simulation of a hydraulic tunnel during standpipe lifting, Tunn. Undergr. Space Technol. 26 (6) (2011) 674–685, https://doi.org/10.1016/j.tust.2011.05.009.
[44] GB/T 50470-2017, 2017. Seismic technical code for oil and gas transmission pipeline engineering. Beijing: China Planning Press.
[45] J. Lubliner, J. Oliver, S. Oller, E. Onat, A plastic-damage model for concrete, Int. J. Solids Struc 25 (3) (1989) 299–326, https://doi.org/10.1016/0020-7683(89)90050-4.
[46] L. Jeeho, L. Gregory, Plastic-damage model for cyclic loading of concrete structures, Eng. Fract. Mech. 124 (8) (1998) 892–900, https://doi.org/10.1061/(ASCE)0733-9399(1998)124:8(892).
[47] GB50010–2010. 2010. Code for design of concrete structures. Beijing: China Architecture and Building Press.
[48] C. Liu, Z. Peng, J. Cui, X. Huang, Y. Li, W. Chen, Development of crack and damage in shield tunnel lining under seismic loading: refined 3D finite element modeling and analyses, Thin Wall Struct. 185 (2023) 110647, https://doi.org/10.1016/j.tws.2023.110647.
[49] H. Yu, C. Cai, A. Bobet, X. Zhao, Y. Yuan, Analytical solution for longitudinal bending stiffness of shield tunnels, Tunn. Undergr. Space Technol. 83 (2019) 27–34, https://doi.org/10.1016/j.tust.2018.09.011.

[50] D. Liu, C. Tian, F. Wang, Q. Hu, J. Zuo, Longitudinal structural deformation mechanism of shield tunnel linings considering shearing dislocation of circumferential joints, Comput. Geotech. 139 (2021) 104384, https://doi.org/10.1016/j.compgeo.2021.104384.
[51] Lu, Y., 2019. Full-scale model test of shield tunnel segment and simulation analysis of circumferential joint. Beijing: China Academy of Railway Sciences.
[52] CJJ/T 289-2018, 2018. Technical standard for maintenance of tunnel structures in urban rail transit. Beijing: China Architecture and Building Press.
[53] X. Bao, H. Yuan, J. Shen, C. Liu, X. Chen, H. Cui, Numerical analysis of seismic response of a circular tunnel-rectangular underpass system in liquefiable soil, Comput. Geotech. 174 (2024) 106642, https://doi.org/10.1016/j.compgeo.2024.106642.
[54] X. Bao, J. Li, J. Shen, X. Chen, C. Zhang, H. Cui, Comprehensive multivariate joint distribution model for marine soft soil based on the vine copula, Comput. Geotech. (2024) 106814, https://doi.org/10.1016/j.compgeo.2024.106814.
[55] J. Shen, X. Bao, J. Li, X. Chen, H. Cui, Study on the mechanism of EPWP dissipation at the joints of shield tunnel in liquefiable strata during seismic events, Soil Dyn. Earthq. Eng. 188 (2025) 109089, https://doi.org/10.1016/j.soildyn.2024.109089.
[56] Y. Yang, B. Zhou, X. Xie, Chao Liu, Characteristics and causes of cracking and damage of shield tunnel segmented lining in construction stage – a case study in Shanghai soft soil, Eur. J. Environ. Civ. Eng. 22 (2017) 213–227, https://doi.org/10.1080/19648189.2017.1356243.